

Amplifier scheme: driven by direct-drive under ~ 10 MJ laser toward inertial fusion energy

Ke Lan (蓝可),* Xiumei Qiao (乔秀梅), and Yongsheng Li (李永升)
Institute of Applied Physics and Computational Mathematics, Beijing 100094, China

Xiaohui Zhao (赵晓晖) and Zhan Sui (隋展)
Shanghai Institute of Laser Plasma, China Academy of Engineering Physics, Shanghai 201800, China

The National Ignition Facility successfully achieved target gain 2.4 thus marginally entering into burn stage. Meanwhile, a recent conceptual design on 10 MJ laser driver [*Matter Radiat. Extremes* **9**, 043002 (2024)] provides a new room for exploring novel target designs and interesting phenomena in a burning plasma after ignition. In this paper, we propose an amplifier scheme with extended burn stage, which includes secondary implosion, generates extremely hot and dense fusion fireball, and produces additional gain. Same as the central ignition scheme used for inertial confinement fusion since 1960s', this new amplifier scheme includes implosion and stagnation, with fusion starting from the central hot spot and serving as a spark plug for ignition. However, the fuel burn in the amplifier scheme is dominated by density and has following characteristics: (1) formation of an extremely compressed shell with a high areal density at stagnation; (2) density dominated ignition and move of fusion peak toward the shell; (3) primary explosion in shell and formation of a fireball in the center; (4) secondary explosion in the extremely hot and dense fireball. The amplifier scheme can be realized either by direct-drive or by indirect-drive. Here, we present a direct-drive amplifier design. A central ignition design is also presented for comparison. From our 1D simulations, the yield released by the amplifier capsule after bangtime is 4.8 times that before, remarkably higher than 1.25 times of the central ignition capsule. The amplifier scheme can be realized at a low convergence ratio, so it can greatly relax the ρRT hot spot condition and the stringent requirements on engineering issues by a high gain fusion. Especially, the fireball lasts for 30 ps, reaching 330 g/cm^3 , 350 keV, 54 Tbar at center when the secondary explosion happens, which leaves an important room for novel target designs towards clean fusion energy.

Fusion energy has been a quest of mankind for more than a half century [1, 2]. Ignition of the National Ignition Facility (NIF) at Lawrence Livermore National Laboratory [3–7] successfully demonstrated the feasibility of inertial confinement fusion (ICF), which ideally positions inertial fusion energy (IFE) as a highly promising approach for energy production. Current record of the target energy gain is $G = 2.4$ on the NIF[8], where G is the ratio of fusion energy output to input laser energy, is far below IFE requirements. While $G > 1$ implies that some fuel is burnt, its amount is small and the burn stage is not well understood. In fact, burn efficiency Φ is a key to increase G . For IFE required high gain, one has to achieve extreme levels of spherical compression of fuel to reach high areal density ρR and high ion temperature T_i for sufficient burn-up. Here, ρ is mass density, and R is radius. For fuel of hydrogen isotopes deuterium and tritium (indicated as symbols D and T, respectively) mainly used in current ICF studies, it requires $\rho R \sim 3 \text{ g/cm}^2$ and $T_i > 4.3 \text{ keV}$ with a density compression of about 1500 or a size convergence ratio of about 35. While, in the central ignition scheme used for ICF since 1960s', the ignition happens in a small central hot spot fuel with mass only a few percent of total fuel, and it is very hard to achieve such high level spherical compression by considering the drive asymmetry [9–14], laser-plasma instabilities [15–17], hydrodynamic instabilities [18–21] and many engineering factors. As a result, it is hard to achieve a burn efficiency higher than 30% in the central ignition scheme of ICF.

Nevertheless, it is interesting to note that the volumetric

reaction rate is proportional to ρ^2 , indicating the role of ρ of the fuel in achieving efficient release of fusion energy[1]. A recent conceptual design of a 10 MJ laser driver [22] provides a room for exploring novel target designs and interesting phenomena in burn stage to achieve high burn efficiency and high gain. In this paper, we will take this advantage of ρ and propose an amplifier scheme, which can generate an extremely hot and dense fusion fireball and produce additional gain after ignition via cascading explosions. This amplifier scheme can be realized either by direct-drive or by indirect-drive. Here, we will present an amplifier design with a spherical capsule containing DT fuel inside an ablator shell of glow discharge polymer plastic (CH) for direct-drive ICF [23–25]. An indirect-driven amplifier design is presented in our separate paper [26].

Before presenting the amplifier scheme, it is worth mentioning the stages of the central ignition scheme [1, 27], including: (1) ablation and implosion; (2) stagnation and formation of a hot spot; (3) ignition in the hot spot; (4) burn and explosion. At stagnation, it generates a highly compressed fuel shell enclosing a hot spot in the center with $\rho_c/\rho_h \sim 10$, where ρ_c and ρ_h are densities of cold shell and hot spot respectively. This scheme has following characteristics: (1) pressure P in hot spot is constant, and both temperature and fusion reaction rate drop sharply when approaching the shell; (2) it has an explosion happening in the central hot spot; (3) whole fuel expands immediately after explosion. The characteristic times include: (1) t_{fuel} , when the released fusion energy is equal the thermal energy deposited in the hot spot, $G_{fuel} = 1$; (2) t_{stag} , stagnation time when kinetic energy of fuel in the shell attains its minimum; (3) t_{ign} , ignition time when fusion energy output equals to input laser energy, $G = 1$; (4) t_{bang} , bang time when

* lan_ke@iapcm.ac.cn

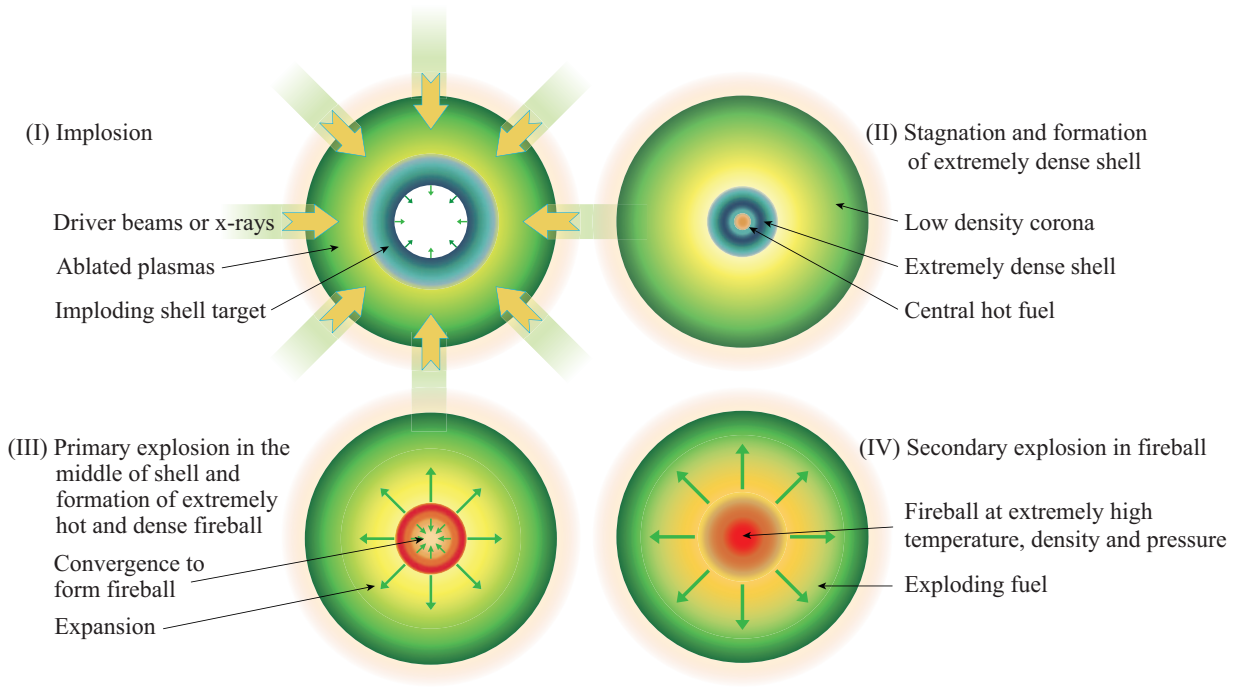


FIG. 1. Principle of the amplifier scheme. Here, we take the style of Fig. 3.1 in Ref. 1

the nuclear reaction rate dN/dt of whole fuel reaches its peak. Here, N is number of neutrons, and t is time.

Same as the central ignition scheme, the amplifier scheme includes implosion, stagnation and ignition, with fusion starting from the central hot spot and serving as a spark plug for ignition. However, the amplifier scheme also includes a phase of secondary explosion and has following characteristics. (1) *Formation of an extremely compressed shell with a high areal density at stagnation.* (2) *Density dominated ignition and move of fusion peak from central region toward the shell.* In this phase, the peaks of pressure and $\frac{dN}{dm dt}$ are dominated by density and move rapidly toward the shell. Here, m is mass, and $\frac{dN}{dm dt}$ is reaction rate per unit mass. (3) *Primary explosion in shell and formation of a fireball in the center.* When the peak of pressure moves to the middle of shell where density peaks, the primary explosion happens inside the extremely dense shell. The primary explosion in shell pushes the inner part of fuel to converge spherically and meanwhile forms a fireball in the center. (4) *Secondary explosion and expansion.* When the inner shock converges at center, the secondary explosion happens inside the extremely hot and dense fuel and produces supplementary fusion gain. Principle of the amplified scheme is given in Fig. 1.

In addition to t_{fuel} , t_{stag} and t_{ign} , the amplifier scheme also has characteristic times of t_{pri} and t_{sec} . Here, t_{pri} is the primary explosion time when $\frac{dN}{dm dt}$ reaches peak in the extremely dense shell, and t_{sec} is the secondary explosion time when $\frac{dN}{dm dt}$ reaches peak at the fuel center. The nuclear reaction rate of whole fuel can reach its peak either at t_{pri} or at t_{sec} , depending on design.

In our direct-driven amplifier design, we consider a 2902- μm -radius spherical cryogenic capsule driven by a 9.46 MJ

laser peaking at 1080 TW. The capsule contains a 6.33 mg DT fuel layer and a 7.02 mg CH outer ablator layer. To compare the different characteristics between the amplifier scheme and the central ignition scheme, we also present a central ignition design, which is a 1663- μm -radius cryogenic capsule with 0.842 mg DT fuel and 1.38 mg CH ablator driven by a 1.6 MJ laser peaking at maximum power of 330 TW. The schematics of two capsules and their drive laser pulses are shown in Fig.2.

Simulations studying one-dimensional (1D) implosion performances were performed with a multi-group radiation hydrodynamic code RDMG, widely used in ICF studies [28–30]. In RDMG, the change rate of E , the internal energy per unit mass of fuel, is written as:

$$\frac{dE}{dt} = W_{dep} + W_m + W_r + W_i + W_e$$

Here, W_{dep} is the power density deposited by fusion products, W_m is the contribution due to mechanical work, W_r is energy lost rate by radiation via bremsstrahlung, and W_e and W_i are lost rates by thermal conduction of electron and ion, respectively. In direct-drive, laser energy can be lost in the following ways. First, part of the laser beams can miss target as the capsule implodes. Second, the laser beams can be refracted in the plasma corona if they are not normal to the capsule surface. Third, the laser absorption can be degraded by cross-beam energy transfer, which can divert energy away from the incoming laser beam into the outgoing rays. In RDMG, only the first two effects are considered and described by means of a 3D ray-tracing algorithm with inverse bremsstrahlung absorption as the main absorption scheme. We take the initial diameter of laser beam as 90% of that of the capsule, then laser energy absorption efficiency is 76.2% for both designs.

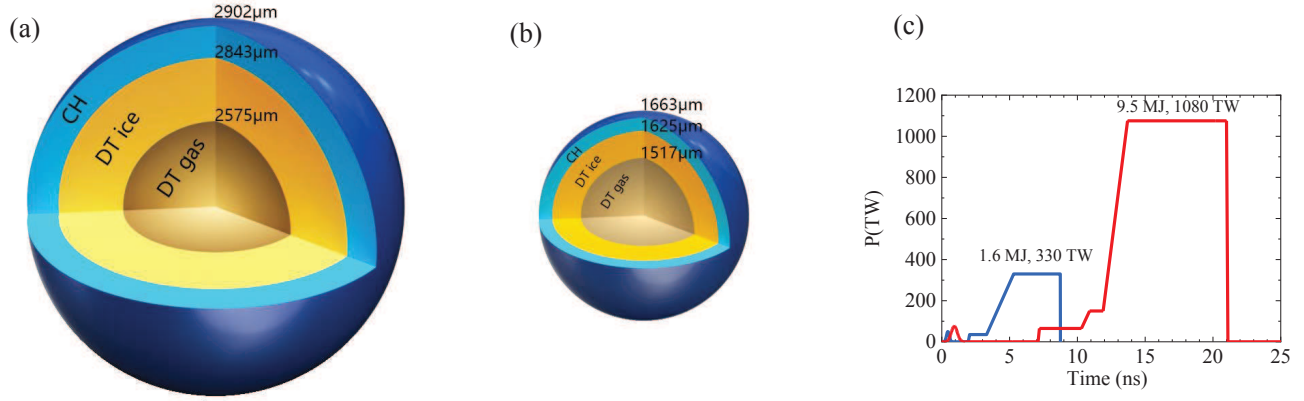


FIG. 2. (Color online) Schematics of the amplifier capsule (a), the central ignition capsule (b), and their drive laser profiles (c).

TABLE I. Comparisons of 1D implosion performances between the amplifier capsule and central ignition capsule. Here, ρR is in g/cm^2 , T in keV, t in ns, velocity in cm/s , mass in mg, E_{abs} refers to the energy absorbed by capsule, and Φ refers to the fraction of burnt fuel. Convergence ratio is defined as the ratio of initial radius of DT gas to hot spot radius at t_{ign} .

Capsule	Central	Amplifier
E_L (MJ), P_L (TW)	1.6, 330	9.46, 1080
E_{abs} (MJ)	1.19	7.24
mass of DT fuel	0.842	6.33
mass of CH ablator	1.38	7.02
α_{if}	2.9	2.37
implosion velocity	4.11×10^7	3.75×10^7
Convergence ratio	19.8	18.6
t_{fuel}	9.302	21.908
t_{stag}	9.376	21.985
t_{ign}	9.404	22.003
t_{bang} or $t_{primary}$	9.457	22.025
$t_{secondary}$	-	22.053
@ t_{fuel} $(\rho R)_h, T_{i,h}$	0.21, 5.3	0.28, 6.7
$(\rho R)_c, T_{i,c}$	0.65, 0.34	1.5, 0.18
@ t_{stag} $(\rho R)_h, T_{i,h}$	0.36, 7.8	0.59, 13
$(\rho R)_c, T_{i,c}$	0.67, 0.65	1.6, 0.34
$\rho_c/\rho_h, \xi$	14, 0.93	28, 3.6
@ t_{ign} $(\rho R)_h, T_{i,h}$	0.46, 9.9	0.82, 17
$(\rho R)_c, T_{i,c}$	0.53, 0.95	1.4, 0.45
@ t_{bang} $(\rho R)_f, T_{i,f}$	0.82, 17	-
	whole fuel burnt	
@ t_{pri} $(\rho R)_h, T_{i,h}$	-	1.6, 42
$(\rho R)_c, T_{i,c}$	-	0.39, 0.36
@ t_{sec} $(\rho R)_f, T_{i,f}$	-	3.2, 85
	-	whole fuel burnt
Φ	16.2%	38.5%
nuclear yield Y_{id} (MJ)	35.5	729
Target gain G	22	77

Inflight fuel adiabat α_{if} is defined as the ratio of pressure to Fermi-degenerate pressure calculated at the density maximum at the time of peak velocity. We have $\alpha_{if} \sim 2.37$ for the amplifier capsule, and $\alpha_{if} \sim 2.9$ for the central ignition capsule.

The amplifier capsule reaches its peak implosion velocity of $3.75 \times 10^7 \text{ cm/s}$ at 21 ns, and it is $4.11 \times 10^7 \text{ cm/s}$ at 8.74 ns for the central ignition capsule. The amplifier design has a slower implosion velocity and a much longer laser pulse. Table I compares the 1D implosion performances between the two capsules.

For the central ignition capsule, $t_{fuel} = 9.302 \text{ ns}$, $t_{stag} = 9.376 \text{ ns}$, $t_{ign} = 9.404 \text{ ns}$, and $t_{bang} = 9.457 \text{ ns}$, with intervals of 74 ps, 28 ps and 53 ps. For the amplifier capsule, $t_{fuel} = 21.908 \text{ ns}$, $t_{stag} = 21.985 \text{ ns}$, $t_{ign} = 22.003 \text{ ns}$, $t_{pri} = 22.025 \text{ ns}$, and $t_{sec} = 22.053 \text{ ns}$, with intervals of 77 ps, 18 ps, 22 ps and 28 ps. The central ignition capsule has one explosion within 53 ps after t_{ign} , while the amplifier capsule has two cascading explosions within 50 ps after t_{ign} . For the amplifier capsule, dN/dt reaches its peak at t_{pri} , i.e., $t_{pri} = t_{bang}$ for this design.

For both designs, a notable temperature difference is observed between ions and electrons in hot spot[31]. At fuel center, we have $T_i/T_e = 118\%$ at t_{fuel} , 106% at t_{stag} , 106% at t_{ign} , and 146% at t_{bang} for the central ignition capsule; and it is 113% at t_{fuel} , 114% at t_{stag} , 122% at t_{ign} , 158% at t_{pri} , and 500% at t_{sec} for the amplifier capsule.

The fusion starts from the central hot spot for both capsules. We define the place as hot spot boundary where $\frac{dN}{dmdt}$ falls to 1% of its peak. We use $(\rho R)_h$ and $T_{i,h}$ to denote the areal density and ion temperature of the hot spot, $(\rho R)_c$ and $T_{i,c}$ for the cold shell, and $(\rho R)_f$ and $T_{i,f}$ for the whole fuel, respectively. The whole fuel is involved in fusion when $(\rho R)_h = (\rho R)_f$. From simulations, that happens at t_{bang} for the central ignition capsule, while for the amplifier capsule it is 17 ps later after t_{pri} , i.e., 11 ps earlier than t_{sec} .

We compare above quantities of the two capsules in Table I. In Fig. 3 and Fig. 4, we present the spatial distributions of T_i , ρ , P and $\frac{dN}{dmdt}$ of the two capsules at their characteristic times, respectively. From Table I, Fig. 3(a) and Fig. 4(a), it is interesting to note the two capsules have a similar hot spot condition at t_{fuel} , with $(\rho R)_h = 0.21 \text{ g/cm}^2$ and $T_{i,h} = 5.3 \text{ keV}$ for the central ignition capsule, and 0.28 g/cm^2 and 6.7 keV for the amplifier capsule. Nevertheless, their cold shells are very different at this time. At t_{fuel} , the central ignition

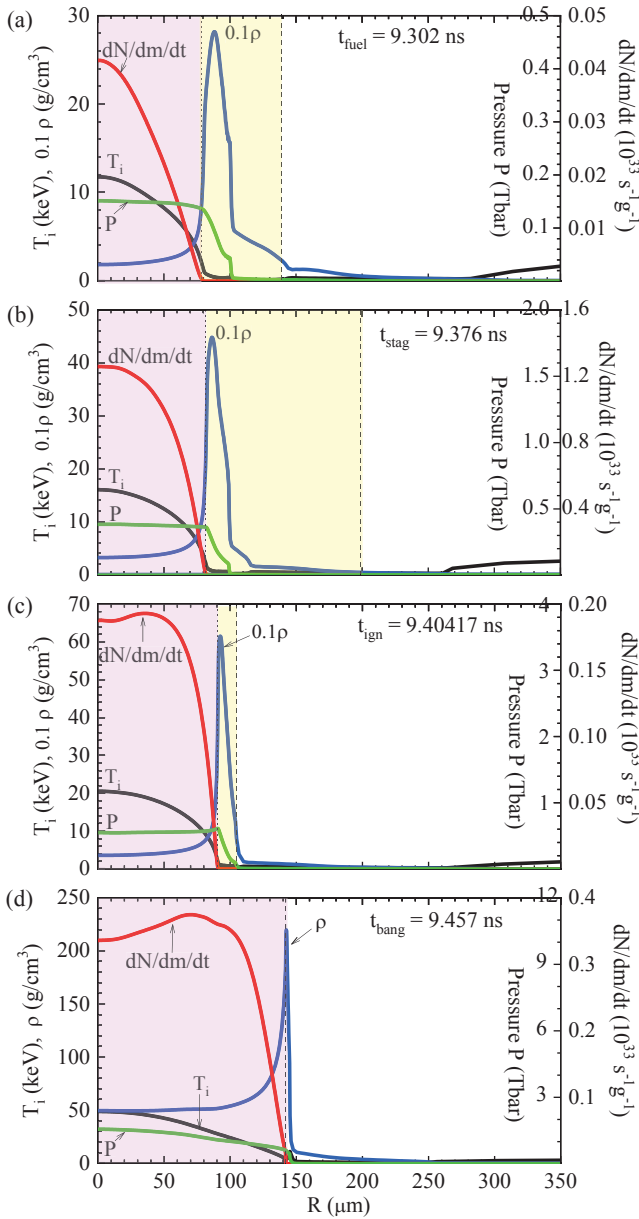


FIG. 3. (Color online) Spatial distributions of T_i (black), ρ (blue), pressure P (green), and reaction rate of neutron per unit mass $\frac{dN}{dm dt}$ (red) at t_{fuel} (a), t_{stag} (b), t_{ign} (c), and t_{bang} (d) of the central ignition capsule. The hot spot and cold shell are marked in lavender and yellow, respectively. The ablator is in white.

capsule has a cold shell with $(\rho R)_c = 0.65 \text{ g/cm}^2$, $T_{i,c} = 0.34 \text{ keV}$ with $\rho_c/\rho_h = 15$, while it is 1.5 g/cm^2 and 0.23 keV with $\rho_c/\rho_h = 25$ for the amplifier capsule. An extremely dense cold shell with a large $(\rho R)_c$ and a low $T_{i,c}$ is a key for the amplifier scheme to stop the α -particles [32] in later ignition and burn phases.

As shown in Fig. 3, the implosion behaviors of the central ignition capsule follow the standard stages of the central ignition scheme. Such as, (1) the central ignition capsule has a constant pressure in hot spot at t_{fuel} , t_{stag} , t_{ign} , and it

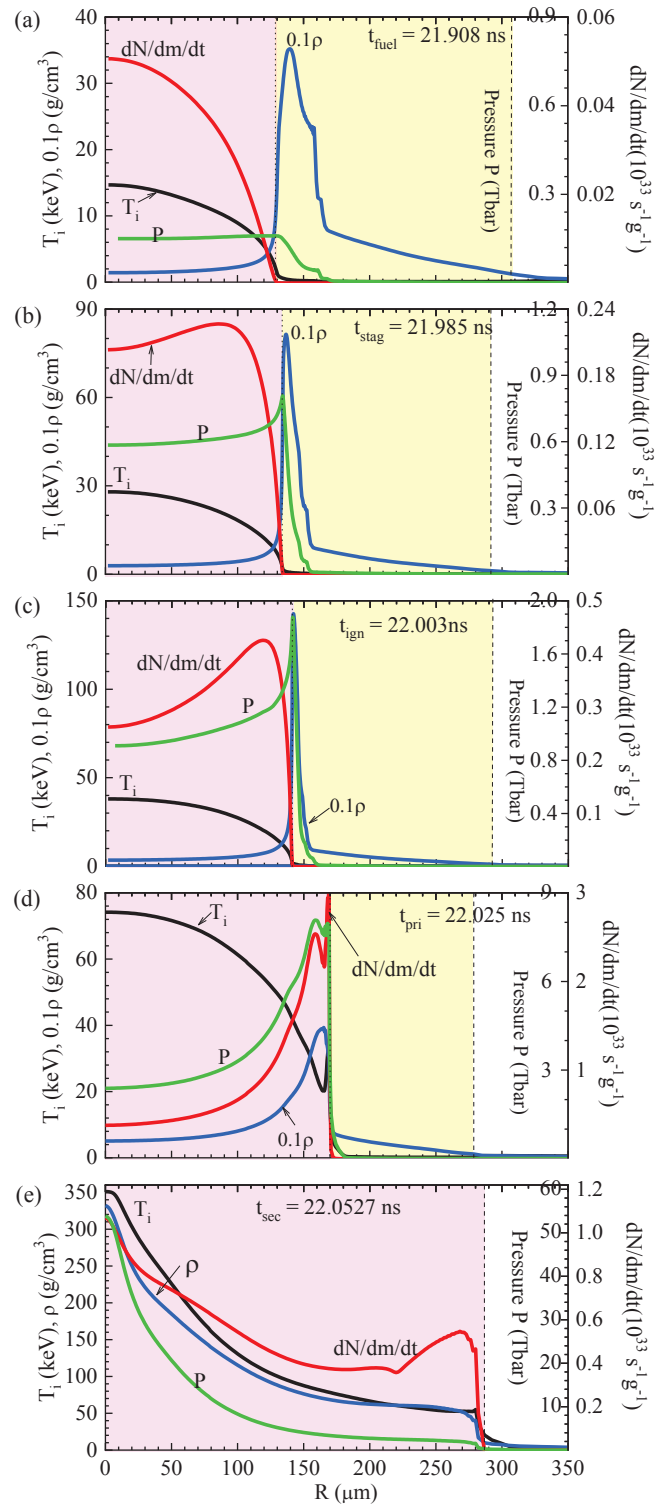


FIG. 4. (Color online) Spatial distributions of T_i (black), ρ (blue), pressure P (green), and reaction rate of neutron per unit mass $\frac{dN}{dm dt}$ (red) at t_{fuel} (a), t_{stag} (b), t_{ign} (c), t_{pri} (d), and t_{sec} (e) of the amplifier capsule. Same as for Fig. 3, the hot spot and cold shell are marked in lavender and yellow, respectively. The ablator is in white.

changes slowly at t_{bang} ; (2) both temperature and fusion reaction rate drop sharply when approaching the shell; and (3) it has only one explosion, and it happens inside the central hot spot. However, the amplifier capsule behaves very different. Though T_i also keeps highest at all times, the amplifier capsule has very different evolutions in P and $\frac{dN}{dmdt}$ because of its extremely dense shell. Below, we focus on Figs. 4(b)-(e) and discuss the characteristics of the amplifier capsule after t_{fuel} .

(1) *Formation of an extremely compressed shell with a high areal density at stagnation.* At t_{stag} , as shown in Fig. 4(a) and Table I, the shell of the amplifier capsule reaches $\rho_c = 810 \text{ g/cm}^3$ with $\rho_c/\rho_h = 28$ and $(\rho R)_c = 1.6 \text{ g/cm}^2$, even denser than at t_{fuel} . At this time, T_i reaches its maximum of 28 keV at center. However, pressure of the amplifier capsule is not constant anymore. Both peaks of P and $\frac{dN}{dmdt}$ move from central region toward the shell. As shown in Fig. 4(b), $\frac{dN}{dmdt}$ reaches its peak of $0.22 \times 10^{33} \text{ s}^{-1} \text{ g}^{-1}$ at $R \approx 86 \mu\text{m}$ where T_i decreases to 21 keV, and P reaches its peak of 0.81 Tbar at 134 μm where T_i drops to 2 keV. It indicates that both pressure and fusion rate are dominated by density after t_{stag} .

(2) *Density dominated ignition and move of fusion peak toward the shell.* At t_{ign} , the amplifier capsule achieves ignition and releases the amount of fusion energy equal to the input laser energy. At the center, as shown in Fig. 4(c), T_i reaches maximum of 38 keV at center. In the middle of the shell where ρ peaks, R is 142 μm with $\rho_c = 1430 \text{ g/cm}^3$, $\rho_c/\rho_h = 42$ and $T_i = 1.42 \text{ keV}$. At this time, though the shell is still very cold, both pressure and neutron yield per unit mass are dominated by the extremely high density of shell and their peaks move rapidly toward the middle of shell. As shown, $\frac{dN}{dmdt}$ reaches its peak of $0.43 \times 10^{33} \text{ s}^{-1} \text{ g}^{-1}$ at 119 μm with $T_i = 20.4 \text{ keV}$, and P reaches its peak of 1.88 Tbar at $R \approx 141 \mu\text{m}$ with $T_i = 1.58 \text{ keV}$. Obviously, the peak of P moves faster than that of $\frac{dN}{dmdt}$, and it almost arrives in the shell middle where ρ peaks at t_{ign} .

(3) *Primary explosion in shell and formation of a fireball in the center.* At t_{pri} , T_i reaches maximum of 74 keV with $\rho = 51 \text{ g/cm}^3$ at center. It is interesting to see, the peaks of P and $\frac{dN}{dmdt}$ simultaneously arrive in the middle of shell where ρ peaks, and it leads the primary explosion. In the shell, ρ reaches its peak of 390 g/cm^3 at 164 μm , with $\rho_c/\rho_h = 8$, $T_i = 21 \text{ keV}$, $P = 8 \text{ Tbar}$, and $\frac{dN}{dmdt}$ reaches $3 \times 10^{33} \text{ s}^{-1} \text{ g}^{-1}$, as shown in Fig. 4(d) and Table I. Note the shell density becomes lower than at t_{ign} because of the expansion after ignition. The primary explosion in the middle of shell violently splits the whole fuel into two parts, pushing the outer part to expand while the inner part to converge spherically to the center. We call this converging central fuel as fireball, and define its boundary as the place where fuel starts to run outwards. At t_{pri} , the fireball mass is 1.93 mg with a 153 μm radius, meaning 30% of whole fuel is involved in the fireball. During converging, the fireball becomes smaller and its mass becomes less, because the relatively high pressure of fireball causes the fuel on the fireball boundary to fly outward.

(4) *Secondary explosion and expansion.* As converging, all of ρ , T_i , P , and $\frac{dN}{dmdt}$ in fireball abruptly increase with their peaks violently moving toward the center. At t_{sec} , 28 ps after

t_{pri} , the fireball converges at the fuel center and the secondary explosion happens. At this time, T_i , ρ , P and $\frac{dN}{dmdt}$ reach their peaks at the center, with 350 keV, 330 g/cm^3 , 54 Tbar, and $1.1 \times 10^{33} \text{ s}^{-1} \text{ g}^{-1}$, as shown in Fig. 4(e). The fireball mass is 0.393 mg, i.e., $\sim 6.2\%$ of whole fuel, with a radius of 82 μm , averaged density of 169 g/cm^3 , averaged ρR of 1.39 g/cm^2 , averaged temperature of 204 keV, and averaged pressure of 19 Tbar. After t_{sec} , the huge pressure at the center violently pushes the whole fuel to expand, and the fireball disappears within 3 ps. Shown in Fig. 5 is the temporal evolutions of R_{fb} , m_{fb} , $T_{i,fb}$ and $(\rho r)_{fb}$ after t_{pri} , where R_{fb} is radius, m_{fb} is mass, $T_{i,fb}$ is averaged temperature, and $(\rho r)_{fb}$ is averaged areal density of the fireball. The radius of whole fuel R_{fuel} is also presented for comparison. Hence, the fireball can last about 30 ps after t_{pri} within a radius of about 150 μm , with temperature increasing as time and peaking at 260 keV.

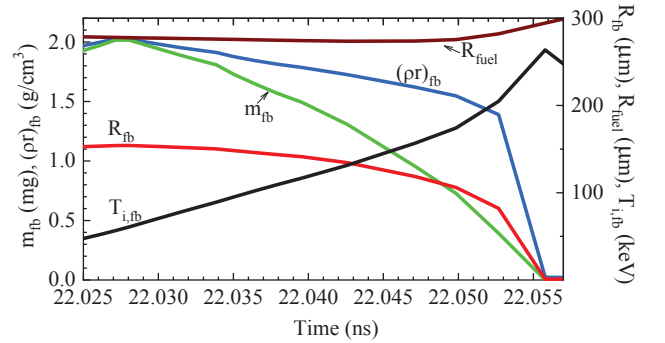


FIG. 5. (Color online) Temporal evolutions of R_{fb} (red), $T_{i,fb}$ (black), m_{fb} (green), $(\rho r)_{fb}$ (blue) and R_{fuel} (wine) after t_{pri} for the amplifier capsule.

It is worth discussing an interesting phenomenon in Fig. 4 (d), in which the burn propagation is seen to be “trapped” inside the sharp boundary located at the outer shell surface. This is because the rate of α -particle local energy deposition exceeding to thermal heat flux at this place. From Ref. 1, we have $W_{dep} \sim T^2$ and $W_e \sim T^{7/2}/\rho R^2$. The explosion can happen at the outer shell surface at t_{pri} when $W_{dep}/W_e > 1$ in case it is W_e which dominates the cooling of the fuel at the outer shell surface. Considering ρ_c/ρ_h is a crucial factor for the amplifier scheme, we can define ρ_c/ρ_h and $\xi = a(\rho R)_c/T_{i,c}^{3/4}$ at stagnation as the trigger criterions for the first explosion in shell. Here, a is a constant to be determined by simulations. Here, we take $a = 1$, with $(\rho R)_c$ in g/cm^2 and $T_{i,c}$ in keV. At t_{stag} , we have $\rho_c/\rho_h = 14$ and $\xi = 0.93$ for the central ignition capsule, and $\rho_c/\rho_h = 28$ and $\xi = 3.6$ for the amplifier capsule, as shown in Table. Hence, both ξ and ρ_c/ρ_h of the amplifier capsule are obviously larger than that of the central ignition capsule.

Shown in Fig. 6 is the temporal evolutions of $T_{i,H}$, ρ_H , $(\rho r)_H$, P , and $\frac{dN}{dt}$ for the two capsules. For the central ignition capsule, as shown, ρ_h , $(\rho r)_h$ and P almost reach their peaks around t_{bang} when $\frac{dN}{dt}$ reach its peak, while $T_{i,h}$ reaches its peak a little later than t_{bang} because of the strong heat

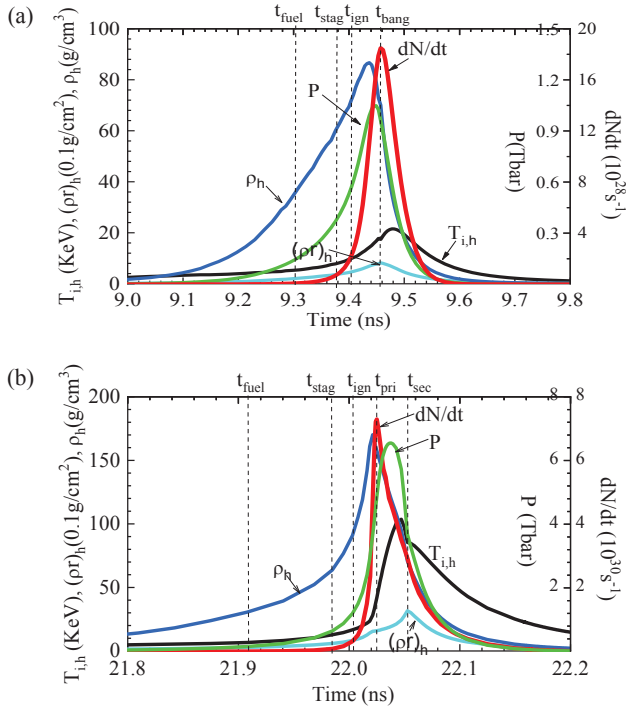


FIG. 6. (Color online) Temporal evolutions of $T_{i,H}$ (black), ρ_H (cyan), $(\rho r)_H$ (blue), P (green) and $\frac{dN}{dt}$ (red) for the central ignition capsule (a) and amplifier capsule (b). Characteristic times are labelled with black dashed lines.

aroused by explosion. In contrast, for the amplifier capsule, ρ_H reaches its peak at t_{pri} while $(\rho r)_H$ is still increasing; and both $(\rho r)_H$ and $T_{i,H}$ reach their peaks around t_{sec} while ρ_H has already dropped to half of its peak. Obviously, the primary explosion of the amplifier capsule is dominated by density, while the secondary explosion is dominated by areal density and temperature.

Presented in Fig. 7 is the temporal evolutions of W_{dep} , W_m , W_r , W_e and W_i of hot spot for the two capsules. As shown, between t_{stag} and t_{ign} , E is mainly raised by W_{dep} while lost by W_m for both capsules. However, it is a little different after explosion happens. For the central ignition capsule, All W_{dep} , $|W_m|$ and $|W_r|$ reach their peaks at t_{bang} when explosion happens, indicating that whole fuel expands immediately after explosion. In contrast, for the amplifier capsule, W_{dep} has two peaks at t_{pri} and t_{sec} , respectively, due to two cascading explosions. In addition, $|W_r|$ of the amplifier capsule greatly increases after t_{pri} and reaches its maximum at t_{sec} ; and $|W_m|$ reaches its 1st peak a short time earlier before t_{pri} and 2nd peak at t_{sec} , due to the strong expansions caused by the two explosions. The contributions of W_i can be completely neglected for both capsules.

It is interesting to compare the temporal evolutions of the fusion rate $\frac{dN}{dt}$ between the two capsules in Fig. 8. As shown, the central ignition capsule has almost the same rising and falling rates of $\frac{dN}{dt}$ around bang time. In contrast, the amplifier capsule has a much slower falling part, due to the contribution of secondary explosion. As a comparison, the yield

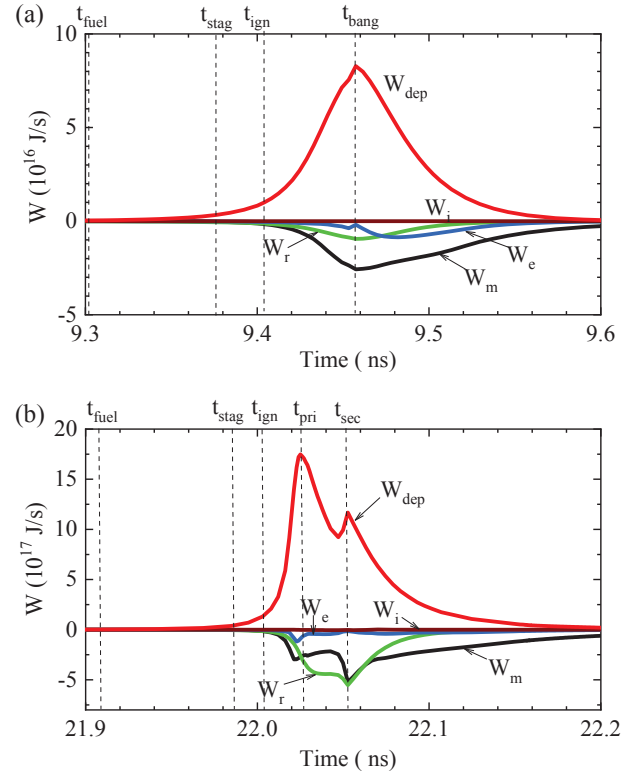


FIG. 7. (Color online) Temporal evolutions of W_{dep} (red), W_m (black), W_r (green), W_e (blue), and W_i (wine) of hot spot for the central ignition capsule (a) and amplifier capsule (b). Times of t_{stag} , t_{pri} and t_{sec} are labelled with black dashed lines.

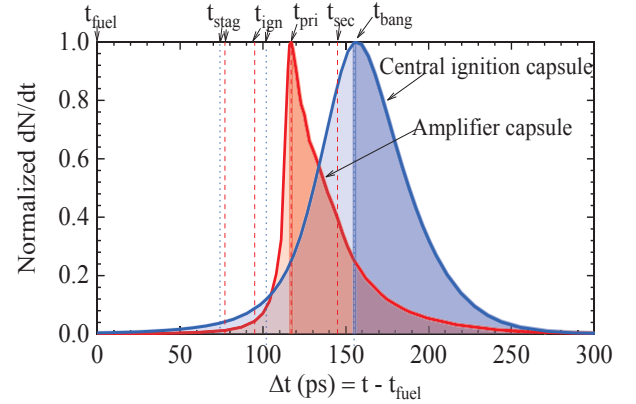


FIG. 8. (Color online) Temporal evolutions of normalized $\frac{dN}{dt}$ for the central ignition capsule (blue) and the amplifier capsule (red). Characteristic times are labelled with blue dotted lines for the central ignition capsule and with red dashed lines for the amplifier capsule.

released by the amplifier capsule after t_{bang} is 4.8 times that before, while it is 1.25 times for the central ignition capsule. It demonstrates that the amplifier capsule releases a significant additional yield in burn stage after ignition. Presented in Fig.9 is spatial distributions of the fraction of burnt fuel Φ at the characteristic times of the two capsules. As shown, Φ at

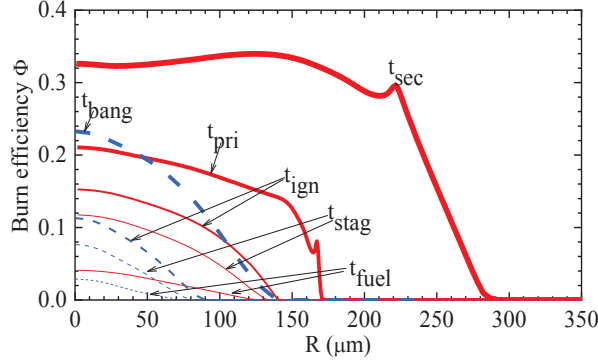


FIG. 9. (Color online) Spatial distribution of the fraction of burnt fuel Φ at the characteristic times of the central ignition capsule (blue dashed lines) and the amplifier capsule (red solid lines).

the center of the central ignition capsule at t_{bang} is even higher than that of the amplifier capsule at t_{pri} , but Φ of the central ignition capsule decreases faster than the amplifier capsule along the radial direction. It is interesting to note that Φ of the amplifier capsule increases remarkably with a very fast burn propagation from t_{pri} to t_{sec} . As a result, we have $\Phi = 38.5\%$ with $Y_{id} = 729$ MJ and $G = 77$ for the amplifier capsule, while $\Phi = 16.2\%$ with $Y_{id} = 35.5$ MJ and $G = 22$ for the central ignition capsule.

To have an overall picture on differences between the amplifier capsule and the central ignition capsule, we present in Fig. 10 the simulated evolutions in space and time of fluid velocity v , ρ , T_e , T_i , P , $\frac{dN}{dmdt}$, W_{dep} and W_m for the two capsules within a time window before stagnation and after explosions. For the central ignition capsule, its stages of (1) ablation and implosion can be seen in Frames a1 and a8, (2) stagnation and formation of a hot spot can be seen in Frames a1 to a8, (3) ignition in hot spot can be seen in Frames a3 to a7, (4) burn and explosion can be seen in Frames a1 to a8. For the amplifier capsule, its stages of (1) ablation and implosion can be seen in Frames b1 and b8, (2) formation of an extremely compressed shell can be seen from Frames b2, (3) density dominated ignition and move of fusion peak toward the shell can be seen from Frames b2 and b7, (4) primary explosion in shell and formation of a fireball in the center can be seen in Frames b1 to b8; (5) secondary explosion in the extremely hot and dense fuel can be seen in Frames b1 to b8. Comparing Frames b3 and b4 with a3 and a4, we can see that temperature in the amplifier capsule increase much more violently during explosions than in the central ignition capsule.

Moreover, we present in Fig. 11 the spacial distributions of ρ and $\frac{dN}{dmdt}$ at t_{bang} for the central ignition capsule and at t_{pri} and t_{sec} for the amplifier capsule. As shown, the two capsules have quite different characteristics in the spacial distribution of ρ and $\frac{dN}{dmdt}$ when their explosions happen. For the central ignition capsule, its explosion is dominated by temperature and happens inside the central hot spot at a relatively low density, which massive fuel mass is wasted in the cold shell of high density. In contrast, the primary explosion of the amplifier capsule is dominated by density and happens inside the

cold shell, leading to almost half of the fuel involved in the explosion. Indeed, the secondary explosion of the amplifier capsule happens in the central region, but with all of density, temperature and pressure reaching their peaks at the center at this time and thus leading to a very efficient burn-up, as shown in Fig. 9. This is quite different from the central ignition scheme which density peaks in the cold shell when its explosion happens.

Finally, it is worth comparing our amplifier scheme with the shock ignition scheme [33] in the following.

- (1) The shock ignition scheme is not the conventional inertial confinement fusion and needs an ignitor shock to heat its central hot spot to ignite the assembled fuel. In contrast, the amplifier scheme is realized fully under inertial confinement, with no need to add any ignitor shock.
- (2) The resulting fuel assembly of the shock ignition features a hot-spot pressure greater than the surrounding dense fuel pressure. In contrast, the amplifier scheme has a surrounding dense fuel pressure greater than the hotspot pressure at and after stagnation.
- (3) The shock ignition needs to launch a spherically converging shock in the latest stage of the implosion to attain a peaked pressure. In contrast, the amplifier scheme does not need to launch such a converging shock in the latest stage of the implosion. Its peak pressure in shell for primary explosion is generated by inertial confinement, and its peak pressure at core for secondary explosion is generated by the primary explosion.
- (4) For the shock ignition, in order to maximize the hotspot peak pressure of the final assembly, the ignitor shock must collide with the return shock inside the dense shell and near its inner surface. In contrast, the amplifier scheme does not have such requirement.
- (5) For the shock ignition, its two new shocks are generated as a result of the collision: an inward and outward moving shock. In contrast, the inward and outward moving shocks of the amplifier scheme is a result of the primary explosion, not a result of collision.
- (6) For the shock ignition, launching a shock during the final stage of the implosion and timing it with the return shock is to generate a nonisobaric assembly. In contrast, the nonisobaric of the amplifier scheme is led by the density dominated nuclear reaction in shell.
- (7) For the shock ignition, because of the relatively high laser intensity 6×10^{15} W/cm² in the spike, a significant amount of hot electrons can be generated by the laser plasma instabilities. In contrast, with no need of such high laser intensity, the amplifier scheme does not have such high laser intensity aroused hot electron issues.
- (8) With no need of the ignitor shock, the amplifier scheme does not have the ignitor shock aroused hydrodynamic instabilities at the end of the acceleration phase.
- (9) The shock ignition is similarly to fast and impact ignition, which shock ignition is induced separately from the compression. In contrast, with no need to add ignitor shock separately, the primary explosion of the amplifier scheme happens automatically inside the extremely compressed shell under inertial confinement.

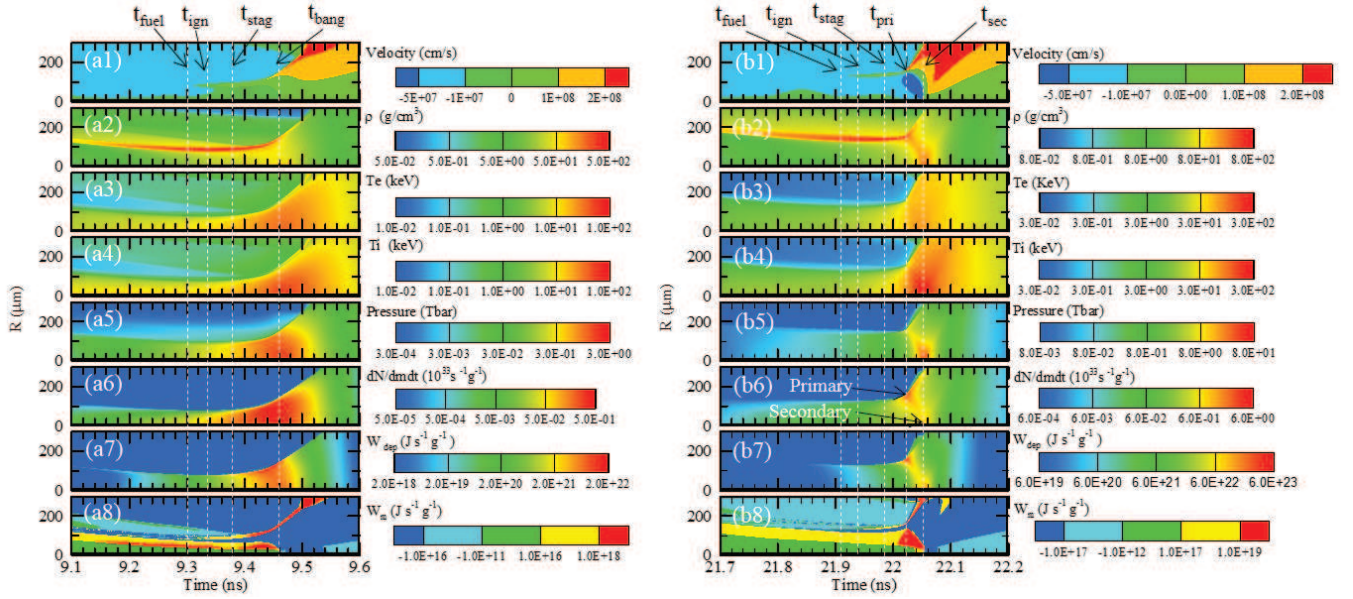


FIG. 10. (Color online) Radial distribution and temporal evolution of v (a1, b1), ρ (a2, b2), T_e (a3, b3), T_i (a4, b4), P (a5, b5), $\frac{dN}{dmdt}$ (a6, b6), W_{dep} (a7, b7), and W_m (a8, b8) for the central ignition capsule (left) and the amplifier capsule (right). Characteristic times are labelled with white dashed lines.

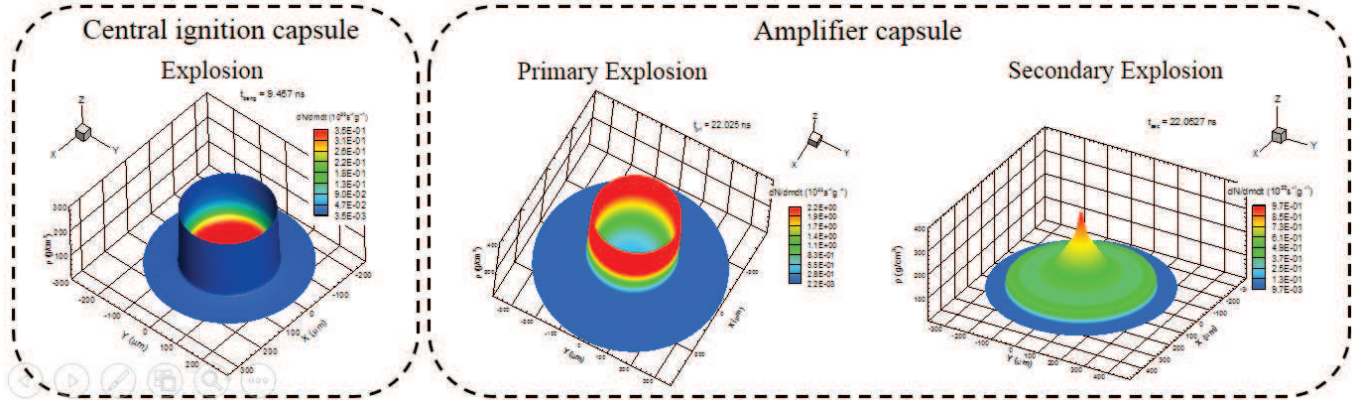


FIG. 11. (Color online) Spatial distributions of ρ (shown by z-axis) and $\frac{dN}{dmdt}$ (shown by color) in x-y plane at t_{bang} of the central ignition capsule (left) and t_{pri} and t_{sec} of the amplifier capsule (right).

In summary, we propose an amplifier scheme to produce additional gain via cascading explosions, which can be realized either by direct-drive or by indirect-drive. In novel scheme, the primary explosion is dominated by density and can be generated at a low convergence ratio, and the secondary explosion is driven directly by the primary explosion. To compare the differences between this new amplifier scheme and the central ignition scheme, we presented the simulations results on a direct-drive amplifier capsule with 6.33 mg DT fuel under a 9.46 MJ laser and a central ignition capsule with 0.842 mg DT fuel under a 1.6 MJ laser. It may seem not a fair comparison because the amplifier capsule uses 5.9 times laser energy of the central ignition capsule, but note it drives the 7.5 times fuel mass. As a result, the yield released by the amplifier capsule after bang time is 4.8 times that before, while it is

1.25 times for the central ignition capsule. This demonstrates that the amplifier capsule can release remarkable additional yield in burn stage after ignition. The amplifier scheme can greatly relax the ρRT hot spot condition and the stringent requirements on target design, target fabrication, and laser engineering issues to achieve a high gain. According to our studies, both ρ_c/ρ_h and $\xi = a(\rho R)_c/T_{i,c}^{\frac{3}{4}}$ can be considered as the trigger criteria for the first explosion in shell, and we are doing the parameter scan to identify them by simulations. We will optimize the amplifier design under a lower laser energy, which is a key for the commercial feasibility of fusion power station. More interesting physics and designs are to be explored in this novel scheme. The extremely hot and dense fireball generated in the amplifier scheme provides a room for novel target designs towards clean fusion energy. Neverthe-

less, the requirement for a high density ratio of the cold shell to the hot spot in the amplifier capsule may be challenging and lead to a hydrodynamic unstable design. We will investigate the beam-to-beam overlapping non-uniformity and hydrodynamic instabilities on the amplifier capsule in our future works.

ACKNOWLEDGMENTS K. L. appreciates Professor

Vladimir Tikhonchuk of the ELI-Beamlines for beneficial discussions on our novel scheme and appreciate S. Atzeni and J. Meyer-ter-Vehn for their very nice book, Ref. 1 in helping to understand and describe the novel phenomena. This work is supported by the National Natural Science Foundation of China (Grant No. 12035002).

-
- [1] S. Atzeni and J. Meyer-ter-Vehn, *The Physics of Inertial Fusion: Beam Plasma Interaction, Hydrodynamics, Dense Plasma Physics* (Clarendon Press, Oxford, 2004); “Report of the Fusion Energy Sciences Workshop on Inertial Fusion Energy”, U. S. Department of Energy, (2023).
- [2] <https://science.osti.gov/-/media/fes/pdf/workshop-reports/2023/IFE-Basic-Research-Needs-Final-Report.pdf>
- [3] H. Abu-Shawareb, R. Acree, P. Adams, J. Adams, B. Addis, R. Aden, P. Adrian, B. B. Afeyan, M. Aggleton, L. Aghaian *et al.*, “Achievement of Target Gain Larger than Unity in an Inertial Fusion Experiment”, *Phys. Rev. Lett.* **132**, 065102 (2024).
- [4] O. A. Hurricane, D. A. Callahan, D. T. Casey, A. R. Christopherson, A. L. Kritcher, O. L. Landen, S. A. Maclaren, R. Nora, P. K. Patel, J. Ralph *et al.*, “Energy Principles of Scientific Breakeven in an Inertial Fusion Experiment”, *Phys. Rev. Lett.* **132**, 065103 (2024).
- [5] M. S. Rubery, M. D. Rosen, N. Aybar, O. L. Landen, L. Divol, C. V. Young, C. Weber, J. Hammer, J. D. Moody, A. S. Moore *et al.*, “Hohlraum Reheating from Burning NIF Implosions”, *Phys. Rev. Lett.* **132**, 065104 (2024).
- [6] A. Pak, A. B. Zylstra, K. L. Baker, D. T. Casey, E. Dewald, L. Divol, M. Hohenberger, A. S. Moore, J. E. Ralph, D. J. Schlossberg *et al.*, “Observations and properties of the first laboratory fusion experiment to exceed a target gain of unity,” *Phys. Rev. E* **109**, 025203 (2024).
- [7] A. L. Kritcher, A. B. Zylstra, R. Weber, O. A. Hurricane, D. A. Callahan, D. S. Clark, L. Divol, D. E. Hinkel, K. Humbird, O. Jones *et al.*, “Design of the first fusion experiment to achieve target energy gain $G > 1$,” *Phys. Rev. E* **109**, 025204 (2024).
- [8] See <https://www.energy.gov/cfo/articles/fy-2025-budget-justification> for more information about the new fusion yield record of 5.2 MJ on the NIF.
- [9] K. Lan, J. Liu, D. Lai, W. Zheng, and X. He, “High flux symmetry of the spherical hohlraum with octahedral 6LEHs at the hohlraum-to-capsule radius ratio of 5.14”, *Phys. Plasmas* **21**, 010704 (2014).
- [10] L. Divol, A. Pak, L. F. Berzak Hopkins, “Symmetry control of an indirectly driven high-density-carbon implosion at high convergence and high velocity,” *Phys. Plasmas* **24**, 056309 (2017).
- [11] S. Craxton, “A new beam configuration to support both spherical hohlraums and symmetric direct drive”. The 62nd Annual Meeting of the American Physical Society Division of Plasma Physics, November 9-13, 2020 in U.S.A.
- [12] K. Lan, Y. Dong, J. Wu, Z. Li, Y. Chen, H. Cao, L. Hao, S. Li, G. Ren, W. Jiang *et al.*, “First inertial confinement fusion implosion experiment in octahedral spherical hohlraum,” *Phys. Rev. Lett.* **127**, 245001(2021).
- [13] K. Lan, “Dream fusion in octahedral spherical hohlraum,” *Matter Radiat. Extremes* **7**, 055701 (2022).
- [14] J. E. Ralph, J. S. Ross, A. B. Zylstra, A. L. Kritcher, H. F. Robey, C. V. Young, O. A. Hurricane, A. Pak, D. A. Callahan, K. L. Baker *et al.*, “The impact of low-mode symmetry on inertial fusion energy output in the burning plasma state,” *Nature Communications* **15**, 2975 (2024).
- [15] D. J. Strozzi, D. S. Bailey, P. Michel, L. Divol, S. M. Sepke, G. D. Kerbel, C. A. Thomas, J. E. Ralph, J. D. Moody, and M. B. Schneider, “Interplay of Laser-Plasma Interactions and Inertial Fusion Hydrodynamics,” *Phys. Rev. Lett.* **118**, 025002 (2017).
- [16] V. T. Tikhonchuk, T. Gong, N. Jourdain, O. Renner, F. P. Condamine, K. Q. Pan, W. Nazarov, L. Hudec, J. Limpouch, R. Liska *et al.* Studies of laser-plasma interaction physics with low-density targets for direct-drive inertial confinement fusion on the Shenguang III prototype. *Matter Radiat. Extremes* **6**, 025902 (2021).
- [17] Y. Guo, X. Zhang, D. Xu, X. Guo, B. Shen, and K. Lan, “Suppression of stimulated Raman scattering by angularly incoherent light, towards a laser system of incoherence in all dimensions of time, space, and angle,” *Matter Radiat. Extremes* **8**, 035902 (2023).
- [18] V. N. Goncharov, S. Skupsky, T. R. Boehly, J. P. Knauer, P. McKenty, V. A. Smalyuk, R. P. J. Town, O. V. Gotchev, R. Betti, and D. D. Meyerhofer, “A model of laser imprinting,” *Phys. Plasmas* **7**, 2062 (2000).
- [19] D. S. Clark, A. L. Kritcher, S. A. Yi, A. B. Zylstra, S. W. Haan, and C. R. Weber, “Capsule physics comparison of National Ignition Facility implosion designs using plastic, high density carbon, and beryllium ablators,” *Phys. Plasmas* **25**, 032703 (2018).
- [20] X. Qiao and K. Lan, “Novel Target Designs to Mitigate Hydrodynamic Instabilities Growth in Inertial Confinement Fusion,” *Phys. Rev. Lett.* **126**, 185001(2021).
- [21] A. Do, C. R. Weber, E. L. Dewald, D. T. Casey, D. S. Clark, S. F. Khan, O. L. Landen, A. G. MacPhee, and V. A. Smalyuk, “Direct measurement of ice-ablator interface motion for instability mitigation in indirect drive ICF implosions,” *Phys. Rev. Lett.* **129**, 215003 (2022).
- [22] Z. Sui and K. Lan, “Driver at 10MJ and 1 shot/30 min for inertial confinement fusion at high gain: Efficient, compact, low-cost, low laser-plasma instabilities, beam color selectable from $2\omega/3\omega/4\omega$, applicable to multiple laser fusion schemes,” *Matter Radiat. Extremes* **9**, 043002(2024).
- [23] J. Nuckolls, L. Wood, A. Thiessen, and G. Zimmerman, “Laser compression of matter to super-high densities: Thermonuclear (CTR) applications,” *Nature* **239**, 139 (1972).
- [24] E. M. Campbell, V. N. Goncharov, T. C. Sangster, S. P. Regan, P. B. Radha, R. Betti, J.F. Myatt, D.H. Froula, M.J. Rosenberg, I.V. Igumenshchev *et al.*, “Laser-direct-drive program: Promise, challenge, and path forward,” *Matter Radiat. Extremes* **2**, 37 (2017).
- [25] V. Gopalaswamy, R. Betti, J. P. Knauer, N. Luciani, D. Patel, K. M. Woo, A. Bose, I. V. Igumenshchev, E. M. Campbell, K. S. Anderson *et al.*, “Tripled yield in direct-drive laser fusion through statistical modelling,” *Nature* **565**, 581 (2019).
- [26] Y. Li, K. Lan, H. Cao, Y.-H. Chen, X. Zhao, and Z. Sui, “Amplifier scheme: increasing burn efficiency via cascading explo-

- sions for inertial confinement fusion,” to be published in *Phys. Plasmas*.
- [27] J. Lindl, S. W. Haan, O. L. Landen, A. R. Christopherson, and R. Betti, “Progress toward a self-consistent set of 1D ignition capsule metrics in ICF,” *Phys. Plasmas* **25**, 122704 (2018).
- [28] T. Feng, D. Lai, and Y. Xu, “An artificial-scattering iteration method for calculating multi-group radiation transfer problem,” *Chin. J. Comput. Phys.* **16**, 199 (1999).
- [29] K. Lan, X. Qiao, P. Song, W. Zheng, B. Qing, and J. Zhang, “Study on laser-irradiated Au plasmas by detailed configuration accounting atomic physics,” *Phys. Plasmas* **24**, 102706 (2017).
- [30] X. Qiao and K. Lan, “Study of high-Z coated ignition target by DCA atomic physics for direct-drive ICF,” *Plasma Phys. Control. Fusion* **61**, 014006 (2019).
- [31] Z. Fan, Y. Liu, B. Liu, C. Yu, K. Lan, and J. Liu, “Non-equilibrium between ions and electrons inside hot spots from National Ignition Facility experiments,” *Matter Radiat. Extremes* **2**, 3 (2017).
- [32] K. Li, and K. Lan, “Escape of α -particle from hot-spot for inertial confinement fusion,” *Phys. Plasmas* **26**, 122701 (2019).
- [33] R. Betti, C. D. Zhou, K. S. Anderson, L. J. Perkins, W. Theobald, and A. A. Solodov, “Shock Ignition of Thermonuclear Fuel with High Areal Density,” *Phys. Rev. Lett.* **98**, 155001 (2007).